

Identifying the Electrostatic and Entropy-Related Mechanisms for Charge-Transfer Exciton Dissociation at Doped Organic Heterojunctions

Wenyue Xue, Yabing Tang, Xiaobo Zhou, Zheng Tang, Hanzhang Zhao, Tao Li, Lu Zhang, Shengzhong (Frank) Liu, Chao Zhao,* Wei Ma,* and Han Yan*

The electron donor/acceptor (D/A) heterojunction is the core for photocharge generation and recombination in organic photovoltaics (OPVs). Developing practical methods for the D/A heterojunction modification remains challenging and is rarely discussed in OPV research. Herein, the roles of molecular doping at the D/A heterojunction in the charge-transfer exciton dissociation and detailed energy loss are investigated, and new insights are gained into the functions of doping on the OPV performance. Heterojunction doping simultaneously enhances all three OPV parameters, especially the short-circuit current (J_{sc}). It is shown that the J_{sc} improvement is due to the combined effects of strengthened electric field and reduced activation energy, which is regulated via an entropy-related mechanism. The performance enhancement is further demonstrated in homojunction devices showing the great potential of interfacial doping to overcome the intrinsic limitation between high J_{sc} and open-circuit voltage (V_{oc}) in OPVs.

1. Introduction

The artificial photoelectric conversion delivers significant application in renewable energy via photovoltaic processes. The main steps in a conversion process include the charge separation at an interface of two materials with different conduction mechanisms and the consequent charge transport. In inorganic photovoltaic devices, free charges are immediately generated upon irradiation and bulk doping controls the conduction behavior on each side of the interface. However, in organic photovoltaics (OPVs) the photogenerated free carriers are associated with Coulomb bound exciton. Therefore, heterojunction between intrinsic D and A materials is necessary, which provides the charge

separation interfaces and charge transporting pathways.^[1,2] The mainstream views on exciton dissociation is based on the concept of charge-transfer (CT) state at an organic heterojunction.^[3–5] The singlet exciton spontaneously transfers to the CT state driven by the potential energy offset at the donor/acceptor (D/A) heterojunction. The CT exciton then evolves to the charge separated (CS) state, which undergoes free carrier formation or decay to the ground state known as geminate recombination. Initially, the endothermic CT–CS transition was thought to be fulfilled via hot CT state where excess vibration energy makes up the potential energy increment.^[6–9] This viewpoint is later challenged by the facts that the excess vibration energy of CT state dissipates faster than the dissociation of CT state^[10] and the free carriers are generated from the thermalized cold CT state regardless of the exciting energy.^[11–13] With a considerable energy offset between the thermalized CT and CS states of 0.3–0.5 eV in state-of-the-art material systems,^[14–17] how to efficiently dissociate the CT exciton into free carriers has been a key issue to achieve high-efficiency OPV devices.


Earlier works have suggested that the CT–CS energetic barrier can be effectively diminished via tuning several factors at the D/A heterojunction, including the electrostatic force, delocalization, disorder, and entropy. The electrostatic force stemming from the charge-quadrupole interaction controls the energy levels of highest occupied molecular orbit (HOMO) and lowest unoccupied molecular orbit (LUMO) as well as the CT state position, thus shifting the balance of CT exciton

W. Xue, Y. Tang, X. Zhou, Dr. C. Zhao, Prof. W. Ma, Prof. H. Yan
State Key Laboratory for Mechanical Behavior of Materials
School of Materials Science and Engineering
Xi'an Jiaotong University
Xi'an 710049, P. R. China
E-mail: zhaochao@mail.xjtu.edu.cn; msewma@xjtu.edu.cn;
mseyanhan@mail.xjtu.edu.cn

Prof. Z. Tang
Center for Advanced Low-dimension Materials
State Key Laboratory for Modification of Chemical Fibers
and Polymer Materials
College of Materials Science and Engineering
Donghua University
Shanghai 201620, P. R. China

H. Zhao, Prof. T. Li
Center of Spintronics and Quantum Systems
State Key Laboratory for Mechanical Behavior of Materials
School of Materials Science and Engineering
Xi'an Jiaotong University
Xi'an 710049, P. R. China

L. Zhang, Prof. S. (F.) Liu
Key Laboratory of Applied Surface and Colloid Chemistry
National Ministry of Education
Shaanxi Engineering Lab for Advanced Energy Technology
School of Materials Science and Engineering
Shaanxi Normal University
Xi'an 710119, P. R. China

 The ORCID identification number(s) for the author(s) of this article can be found under <https://doi.org/10.1002/adfm.202101892>.

DOI: 10.1002/adfm.202101892

to free carrier generation.^[18,19] Delocalization includes both intramolecularly and intermolecularly extended π -electron distribution with larger electron-hole pair distance, and thus effectively decreases the CT exciton binding energy.^[20–23] The energetic disorder leads to broadened density of states (DOS) in organic semiconductors.^[24–26] During the CT exciton dissociation, carriers hop to the states below the center of DOS of transporting energy and therefore disorder liberates the CT exciton. The entropy increases the number of available states to accommodate the electron and hole that make up the CT exciton. Larger entropy means more states for carriers to stay, which reduces the free energy of CT-CS transition according to Gibbs equation.^[27–30] Previous studies have shown that all abovementioned properties are closely related to the local morphology of crystallinity, mixing ratio, and molecular orientation at the D/A heterojunction.^[31–34] The complexity in local morphology regulation and characterization hinders the rational optimization of heterojunction properties in OPVs. Therefore, it's urgent to develop a morphology independent strategy aiming at improving the electronic properties at the D/A heterojunction.

Intuitively, the direct way to tune the electronic properties is to place or take off electrons in the semiconductor, as known as doping.^[35] Doping varies the carrier density in orders of magnitude and correspondingly shifts the Fermi level (E_F) position. Recently, the bulk doping has been adopted in the OPV research. The consequent trap-filling,^[36–38] better charge transport,^[39,40] and morphology optimizations^[41–43] are found to contribute to the enhancement of photovoltaic performances. Going a step further, we intentionally dope the organic heterojunction where

the photocharge generation and recombination take place. We hypothesize that the heterojunction doping potentially benefits the OPV devices in three aspects. First, doping enhances the interfacial electric field by storing extra charges at the heterojunction, which is good for overcoming the Coulomb binding energy. Second, the ability to tune the energetic landscapes by doping may directly alter the CT state position, and thermodynamically change the photovoltaic process at the D/A heterojunction. Last but also the most promising thing is that the heterojunction doping provides more states to accommodate the free carriers, which is likely to improve charge generation yield via entropy gain. Fascinated by all these attractions, we conduct our study on the heterojunction doping in OPVs. We discuss how this leads to improved photovoltaic performances and show that it is generally applicable to multiple types of material combinations.

The aim of this study is to comprehensively understand the heterojunction doping and evaluate it as a practical strategy in OPV optimization. A model device based on the planar heterojunction (PHJ) structure is used to exclusively investigate the effect of doping free from complex morphology. With confirmed electron transfer from the polymer donor (poly[(2,6-(4,8-bis(5-(2-ethylhexyl)thiophen-2-yl)-benzo[1,2-b:4,5-b']dithiophene))-alt-(5,5-(1',3'-di-2-thienyl-5',7'-bis(2-ethylhexyl)benzo[1',2'-c:4',5'-c']dithiophene-4,8-dione))] (PBDB-T) to the *p*-dopant 1,3,4,5,7,8-hexafluoro-tetracyanonaphthoquinodimethane (F6TCNNQ) (Figure 1a), the heterojunction doping simultaneously improves all three photovoltaic parameters especially the J_{sc} . We find that the upward CT state movement together with

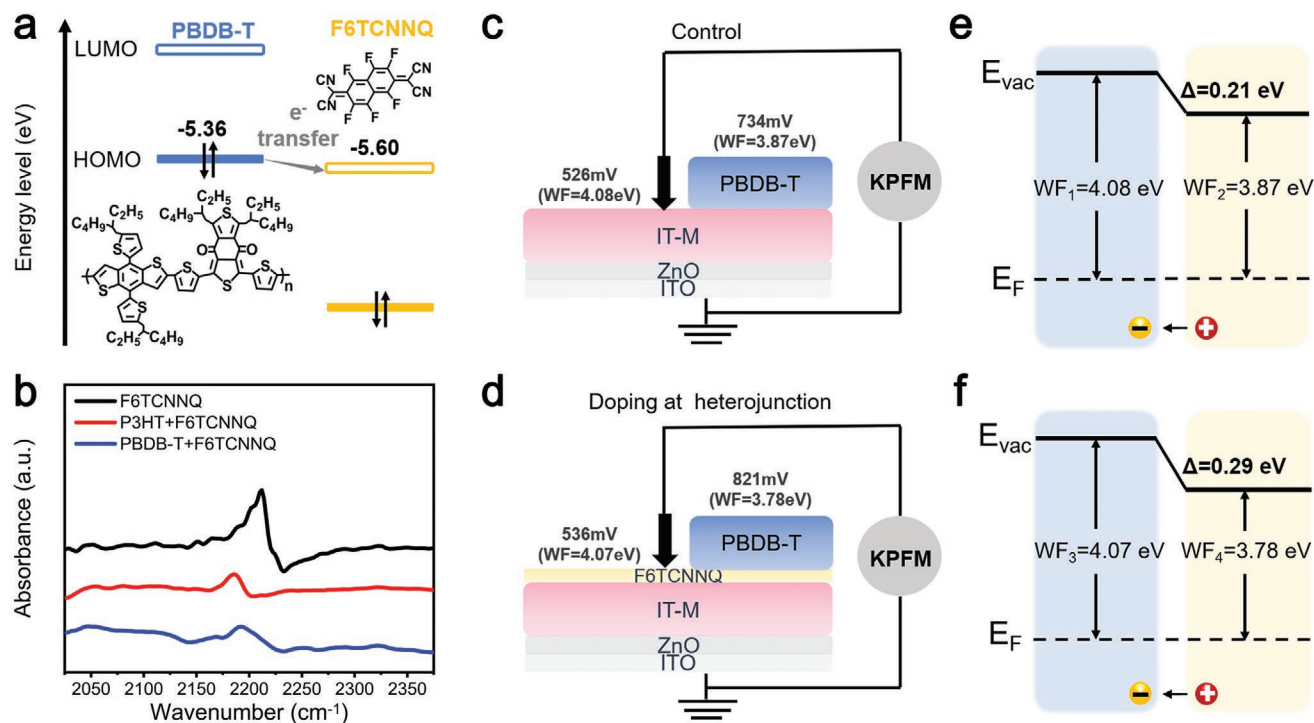


Figure 1. a) The chemical structures of PBDB-T and F6TCNNQ with specific values of HOMO and LUMO energy levels. b) The FTIR spectrum of F6TCNNQ, P3HT with 5 mol% F6TCNNQ (1 dopant per 20 repeat units of the polymer), and PBDB-T with 10 mol% F6TCNNQ films. c,d) KPFM setups of the PBDB-T/IT-M bilayer films: control (c); heterojunction doping (d) at optimum device condition. e,f) The heterojunction energy level diagrams of PBDB-T/IT-M bilayer films corresponding to (c) and (d).

the lower non-radiative recombination is responsible for the slightly higher V_{oc} . A combination of stronger electric field and entropy gain due to heterojunction doping suffices to produce the $\approx 20\%$ J_{sc} increment. The generality of interfacial doping is further examined in two more examples possessing either a heterojunction with larger LUMO offset or even a homojunction with zero energy offsets at both of LUMO and HOMO. Inserting an ultrathin dopant layer leads to enhanced J_{sc} in both cases.

2. Results and Discussion

2.1. Heterojunction Doping Strategy

Herein, we first developed a heterojunction doping strategy that effectively dopes the interface only without dopant diffusion that leads to bulk doping in device. Since dopants stay at heterojunction interface, the CT between dopant and donor (or acceptor) builds up an electric field and thus modifies the energy level alignment over the heterojunction. We employed photoactive blend of a non-fullerene acceptor 3,9-bis(2-methylene-(3-(1,1-dicyanomethylene)-5-methylindanonone))-5,5,11,11-tetra(4-hexylphenyl)dithieno[2,3-d:20,30-d0]sindaceno[1,2-b:5,6-b0]dithiophene (IT-M) (Figure S1, Supporting Information) with the polymer donor PBDB-T. For dopant, we used F6TCNNQ to *p*-doped PBDB-T, since electron transfer from PBDB-T to F6TCNNQ is expected according to the energy levels diagrams (Figure 1a). Effective *p*-doping is confirmed by the peak shift in the Fourier transform infrared (FTIR) spectra of the $\text{C}\equiv\text{N}$ peak (Figure 1b).^[44] The higher wavelength position of the doped PBDB-T film than the doped P3HT film indicates that the partial CT occurs between PBDB-T and F6TCNNQ, resulting in the formation of charge transfer complex (CTC).^[45] To lend more supports on the partial CT between PBDB-T and F6TCNNQ, we provide the absorption and ultraviolet photoelectron spectroscopy (UPS) spectra (Figure S2, Supporting Information). In the absorption spectrum, we observe two new peaks at 924 and 1164 nm in the infrared region which can be ascribed to the transitions of HOMO \rightarrow LUMO and HOMO-1 \rightarrow LUMO in the charge CTC.^[46] After F6TCNNQ doping, the HOMO position of PBDB-T film goes deeper from -4.62 to -5.12 eV, which is explained by the hybridization of dopant's LUMO and polymer's HOMO.^[47] The influence of molecular doping at the D/A heterojunction is then examined by fabricating the bilayer films as described (Figure S3, Supporting Information).^[37] Any morphological alterations after the deposition of F6TCNNQ layer are excluded as evidenced by grazing incident wide-angle X-ray scattering (GIWAXS) characterizations (Figures S4 and S5 and Table S1, Supporting Information).

Charges transfer across the D/A heterojunction, building up a potential step to form the energy level alignment at the vacuum levels. Inserting a dopant layer may enlarge the offset of vacuum levels. To examine the energy level alignment at the D/A heterojunction, we used Kelvin probe force microscopy (KPFM) to map the surface potential (Figure S6, Supporting Information).^[48,49] The experimental setups are schemed in Figure 1c,d. For the control sample, scanning the PBDB-T surface produces an average contact potential of 734 mV, which is

higher than the value of 526 mV on the IT-M surface (Figure 1c). The energy level alignment at the undoped PBDB-T/IT-M heterojunction builds up a potential of 208 mV with the positive charge end pointing toward the PBDB-T layer. Inserting an ultrathin F6TCNNQ layer at the heterojunction increases the contact potential of PBDB-T to 821 mV, subtracts the IT-M value of 536 mV, and the built-in potential (V_{bi}) is enlarged to 285 mV (Figure 1d). The specific energy level alignments for control and heterojunction doped samples are schemed in Figure 1e,f. Doping results in a heterojunction potential increment of 77 mV by interfacial energy alignment, which is beneficial for CT exciton dissociation in PHJ devices. The detailed mechanism will be discussed later in the text.

2.2. Solar Cell Characteristics

We next fabricate PHJ devices to examine the effects of molecular doping at the D/A heterojunction on the photovoltaic performance. PHJ devices with constant film thickness (≈ 30 nm for D and A layers) were characterized in terms of J_{sc} , V_{oc} , and fill factor (FF) (Figure 2a). Excitingly, we find that spin-coating an ultrathin layer of F6TCNNQ at the D/A heterojunction (0.001 mg mL⁻¹ in ethanol) strikingly enhances the J_{sc} by over 20%, from an average value of 2.03 to 2.44 mA cm⁻² (Table 1). Simultaneously, V_{oc} and FF also benefit from the optimum heterojunction doping. The average V_{oc} increases from 0.90 to 0.92 V, and the FF becomes slightly better from 64.5% to 66.4% (Table 1). At the same time, spin-coating the same amount of ethanol solvent makes little performance enhancement when compared with the heterojunction doped devices, which excludes the effects of solvent treatment on performance increment. The significant enhancement of J_{sc} is supported by the external quantum efficiency (EQE) measurement, where the calculated J_{sc} are 2.03 and 2.40 mA cm⁻² for the control and heterojunction doped samples, respectively (Figure 2b). Further increasing the concentration of F6TCNNQ solution to 0.01 mg mL⁻¹, the average power conversion efficiency (PCE) drops from 1.49% to 1.27%, which is mainly a result of FF losses, probably due to larger resistance introduced by a thick dopant layer. Consistent with our previous report, adding the F6TCNNQ in PBDB-T layer does not help the photovoltaic performance (Figure S7 and Table S2, Supporting Information).^[37] Furthermore, we used 7,7,8,8-tetracyanoquinodimethane (TCNQ) instead of F6TCNNQ, which is similar in molecular structure but lack of doping ability due to the mismatching energy levels (Figures S1 and S8 and Table S3, Supporting Information). Spin-coating 0.001 mg mL⁻¹ TCNQ ethanol solution at the D/A heterojunction produces an average J_{sc} of 2.03 mA cm⁻² resembling the control devices. This excludes the spacer effect introduced by a very thin interlayer on improved device performances in previous reports.^[50,51] In addition, we compare the device performances with the results of other PHJ devices by inserting a dipole layer at the D/A heterojunction.^[52-54] It seems that the dipole layer adversely affects the J_{sc} (Figure S9, Supporting Information), which also rules out the influence of dipole modification and reconfirms an undoubted doping effect, as the reason for better photovoltaic performance with heterojunction doping.

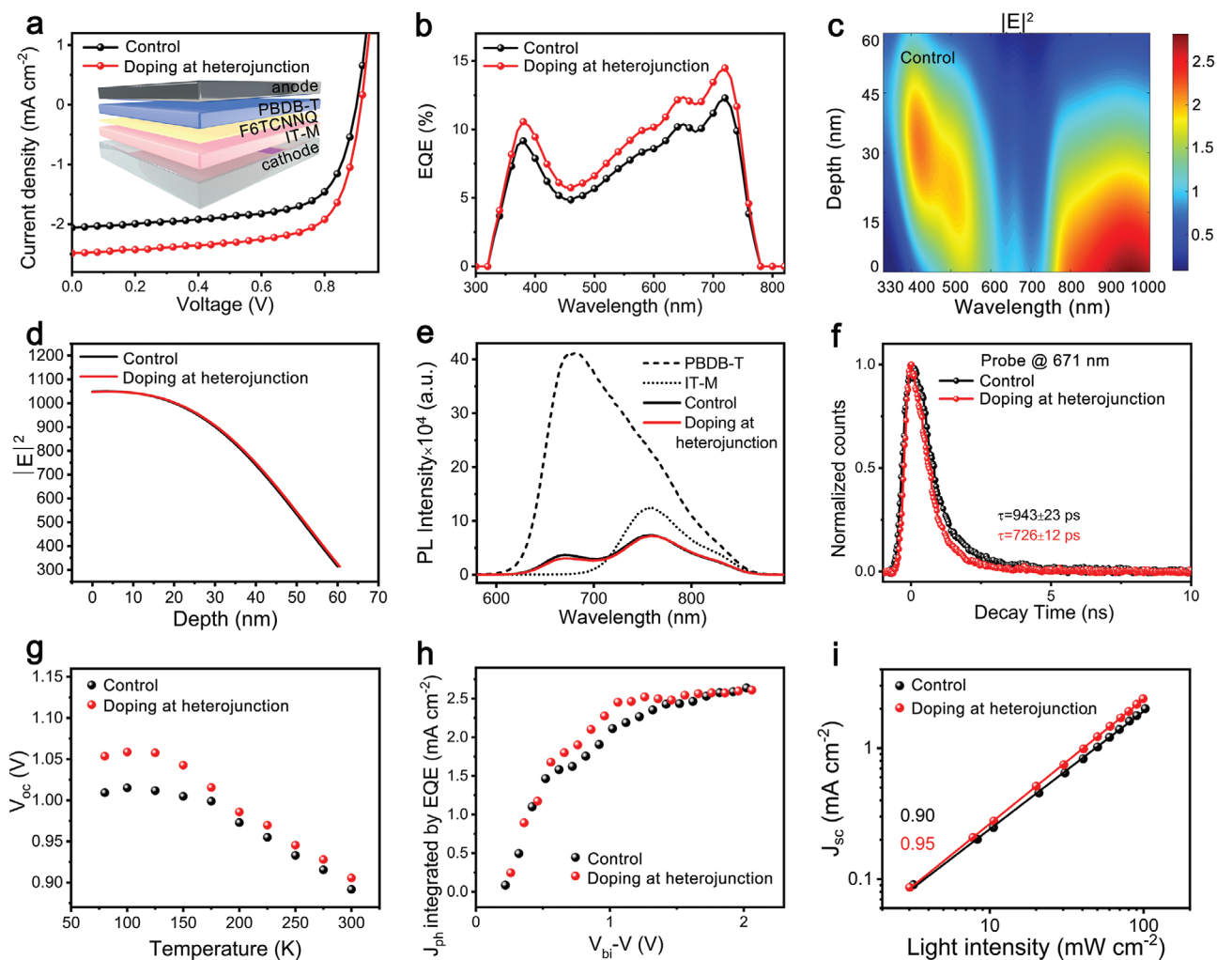


Figure 2. a) J - V curves of PBDB-T/IT-M PHJ devices; the inset demonstrates the device structure. b) The corresponding EQE curves. c) Simulated $|E|^2$ distribution inside the active layer of PHJ device via optical transfer-matrix model (assuming an interlayer thickness of 0.5 nm). d) Comparison of the depth dependent integrated $|E|^2$ in PHJ devices. e) The steady state PL spectra of PHJ films (excited at 510 nm). f) The TRPL spectra of PHJ films (excited at 510 nm and probed at 671 nm). g) Plots of V_{oc} as a function of temperature under 1 Sun irradiation from 80 to 300 K. h) Bias dependent integrated J_{ph} from EQE. The applied bias ranges from -1 to 0.8 V with an interval of 0.1 V, and the applied bias is corrected by the built-in potential. i) J_{sc} plots against light intensity.

2.3. Opto-Electric Properties of Planar Heterojunction Devices

The photo-charge generation is a step-wise process, where the photon distribution in real devices is the prerequisite for the following exciton diffusion and dissociation. As discussed, an added layer in device may function as an optical spacer layer and thus alter the photon distribution throughout the active layer.^[55] To rule out the optical effects, we simulated the

photon distribution in PHJ device using the well-established optical transfer-matrix model (see details in Experimental Section).^[56,57] The light incides normal to the bottom cathode of ITO/ZnO, same as the device testing condition, and the interface between ZnO and IT-M is defined as the zero position. The simulated contours of the optical electric field ($|E|^2$) in the bilayer structure at AM 1.5 G are summarized in Figure 2c,d, and the corresponding optical parameters are

Table 1. Photovoltaic performances of PBDB-T/IT-M in PHJ device structure (The average values are obtained from 10 devices).

Conditions		$V_{oc\ max}$ [V]	$V_{oc\ avg}$ [V]	FF_{max} [%]	FF_{avg} [%]	$J_{sc\ max}$ [mA cm^{-2}]	$J_{sc\ avg}$ [mA cm^{-2}]	PCE_{max} [%]	PCE_{avg} [%]
Control	None	0.90	0.90 ± 0.004	66.2	64.5 ± 1.0	2.06	2.03 ± 0.03	1.23	1.17 ± 0.03
	Ethanol	0.90	0.90 ± 0.003	63.7	64.1 ± 1.0	2.14	2.08 ± 0.05	1.23	1.20 ± 0.03
Doped	$0.0001\ \text{mg mL}^{-1}$	0.91	0.91 ± 0.006	67.0	65.2 ± 0.9	2.16	2.18 ± 0.04	1.31	1.29 ± 0.03
	$0.001\ \text{mg mL}^{-1}$	0.92	0.92 ± 0.003	68.6	66.4 ± 1.5	2.49	2.44 ± 0.04	1.56	1.49 ± 0.05
	$0.01\ \text{mg mL}^{-1}$	0.91	0.90 ± 0.005	60.5	60.6 ± 1.3	2.37	2.32 ± 0.05	1.31	1.27 ± 0.03

listed in Figure S10, Supporting Information. The $|E|^2$ distributions are almost the same for the control and heterojunction doped samples, therefore we exclude the possibility of photon absorption induced photocurrent change. Both of the PHJ films show extensive photoluminescence (PL) quenching due to CT, while adding an F6TCNNQ layer increases the quenching extent (Figure 2e). We further monitored the exciton decay dynamics at 671 nm by time-resolved photoluminescence (TRPL) spectroscopy. The exciton lifetime extracted by exponential fitting decreases from 943 ± 23 to 726 ± 12 ps with heterojunction doping (Figure 2f). The higher quenching extent with faster decay dynamics highlights the advantages of doping at PBDB-T/IT-M heterojunction on the J_{sc} enhancement with facilitated exciton dissociation.

We then examined the effect of heterojunction doping on device built-in potential. As shown in Figure 2g, the $V_{bi}^{[58]}$ of heterojunction doped devices increases from 1.02 to 1.06 V, which is consistent with the KPFM results. This confirms our hypothesis on the modification of energy level alignment over the heterojunction. To more accurately correlate the J_{sc} variation with doping modified PBDB-T/IT-M heterojunction, we performed a series of EQE measurements under varying biases. Since the PHJ devices were tested under weak light intensity and large reverse bias, the bimolecular recombination in charge transport and charge collection is negligible. Therefore, these measurements provide insights in the balance between charge generation and geminate recombination right at the heterojunction. The bias dependent EQE curves are listed in Figure S11,

Supporting Information, and the integrated photocurrent (J_{ph}) curves are summarized in Figure 2h. Though the integrated J_{ph} of the control and heterojunction doped devices saturate at the same value when $V - V_{bi} > 1.5$ V, the doped device shows roughly 13% higher J_{ph} when operated under the same bias at near J_{sc} condition. Noted that this 13% increment is lower than the total 20% enhancement in J_{sc} , we therefore deduce that the internal electric field is not the only origin for J_{sc} improvement. We also evaluate the role of counter ion F6TCNNQ $^{\delta-}$ ($\delta < 1$) at the D/A heterojunction. Since the light intensity dependent coefficient α ($J_{sc} \propto \text{sun}^\alpha$) of doped heterojunction device is higher than the control device (0.95 vs 0.90), we conclude that the F6TCNNQ $^{\delta-}$ ($\delta < 1$) passivates the traps at the interfaces at low content, and it behaves as neither the space charge nor the charge trap (Figure 2i).

2.4. Energy Loss in Planar Heterojunction Devices

The ultimate V_{oc} is obtained by considering three parts of voltage losses, including the offset between the optical bandgap and CT state position (E_{CT}), the radiative recombination, and the non-radiative recombination.^[32,59,60] The optical bandgap for PBDB-T/IT-M bilayer film is determined as 1.69 eV by the intersection of the normalized absorption spectrum and emission spectrum of the pristine films (Figure 3a).^[61] The E_{CT} is routinely studied with the sensitive EQE (sEQE), where it is defined as a shoulder at subbandgap energies. The E_{CT} is

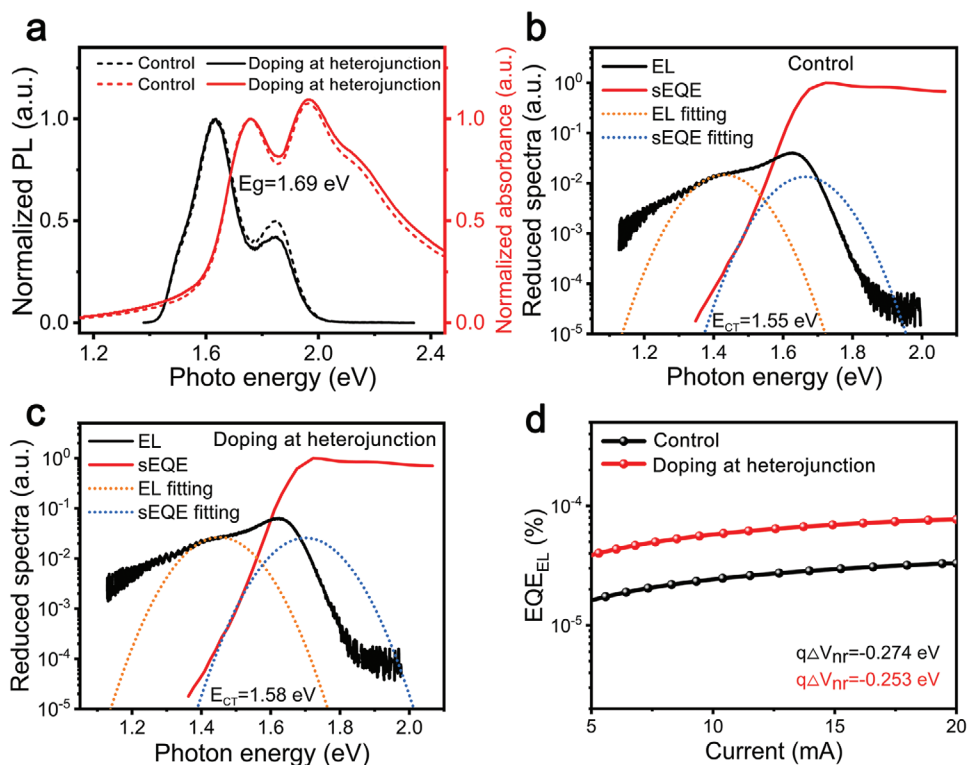


Figure 3. a) The PL spectra (black lines) and absorption spectra (red lines) of PBDB-T/IT-M bilayer films. b,c) Characterization of the CT state in PHJ devices: control (b) and doping at heterojunction (c) by simultaneous fitting of the subbandgap absorption and EL spectra. d) EQE_{EL} measurements of PBDB-T/IT-M PHJ devices.

extracted by a simultaneous fit to the measured absorption spectrum (Equation (1)) and emission spectrum (Equation (2)).^[60]

$$\sigma(E)E = \frac{f}{\sqrt{4\pi\lambda kT}} \exp\left(\frac{-(E_{CT} + \lambda - E)^2}{4\lambda kT}\right) \quad (1)$$

$$\frac{I(E)}{E} = \frac{f}{\sqrt{4\pi\lambda kT}} \exp\left(\frac{-(E_{CT} - \lambda - E)^2}{4\lambda kT}\right) \quad (2)$$

where E represents photon energy; λ , reorganization energy; f is a factor proportional to the number of CT states and the square of their coupling matrix element with the ground state; k denotes Boltzmann's constant. We obtain E_{CT} values of 1.55 and 1.58 eV for the control and heterojunction doped devices (Figure 3b,c). The energy loss due to recombination can be divided into radiative (ΔV_{rad}) and non-radiative terms ($\Delta V_{non-rad}$). The non-radiative voltage loss is calculated by the EQE of electroluminescence (EQE_{EL}).^[60]

$$\Delta V_{non-rad} = -\frac{kT}{q} \ln(\text{EQE}_{EL}) \quad (3)$$

The heterojunction doped device exhibits a non-radiative loss of 0.253 eV, which is 0.021 eV lower than that of the control device (Figure 3d). Thus, the ΔV_{rad} are calculated to be 0.376 and 0.407 eV for control and heterojunction doped PHJ devices, respectively. The detailed data for energy loss are summarized in Table S4, Supporting Information. Having quantified all three parts of the voltage loss, we conclude that the upward CT state movement and the reduced non-radiative recombination are responsible for higher V_{oc} in OPV devices. The higher CT position also reduces the electronic coupling between the CT state and ground state, thus shifting the generation-recombination balance toward free carrier formation. The balance shift is supported by the transient photovoltage (TPV) measurement, where the doped device gives a carrier lifetime of 33 μ s, which is obviously longer than the control device (17 μ s) at 0.82 V bias (Figure S12, Supporting Information).

2.5. Exciton Dissociation Efficiency

Having answered the question on enhanced V_{oc} after heterojunction doping, we next turn to understand the most exciting J_{sc} improvement. To understand the origin of J_{sc} increment, we applied the standard effective exciton dissociation probability

$$P = \frac{k_{diss}}{k_{diss} + k_{rec,eff}}$$

model, to evaluate the effect of internal electric field and activation energy on J_{sc} in a bilayer structure, where k_{diss} is the exciton dissociation rate and $k_{rec,eff}$ is the effective exciton recombination rate.^[62] In planar heterojunction, electrons and holes transport in pure acceptor or donor layers with very low carrier recombinations after exciton separation. Therefore, the exciton dissociation probability, P , at PHJ equals to internal quantum efficiency (IQE) (Figure S13, Supporting Information), and thus represents for J_{sc} of the device. According to Onsager–Braun model, the dissociation rate constant k_{diss} of exciton can be expressed as

$$k_{diss}(E_a, E, T) = k(0 \text{ eV}, 0 \text{ V}, T) e^{-\frac{E_a}{kT}} J_1 \left[2\sqrt{2(-b)^{\frac{1}{2}}} \right] / \sqrt{2(-b)^{\frac{1}{2}}} \quad (4)$$

where J_1 is the Bessel function of order one, $b = \frac{e^3 E}{8\pi\epsilon_r \epsilon_0 k^2 T^2}$ and $k(0 \text{ eV}, 0 \text{ V}, T)$ is the dissociation rate with no barrier for dissociation and zero electric field. The J_{sc} increment is therefore a product of internal electric field and activation energy. The effective increment of dissociation rate is expressed as

$$\frac{k_{diss,doped}(E)}{k_{diss,control}(E)} = \frac{J_1 \left[2\sqrt{2(-b_{doped})^{\frac{1}{2}}} \right] / \sqrt{2(-b_{doped})^{\frac{1}{2}}}}{J_1 \left[2\sqrt{2(-b_{control})^{\frac{1}{2}}} \right] / \sqrt{2(-b_{control})^{\frac{1}{2}}}} \cdot e^{-\Delta E_a/kT} \quad (5)$$

where $\frac{J_1[2\sqrt{2(-b_{doped})^{\frac{1}{2}}}] / \sqrt{2(-b_{doped})^{\frac{1}{2}}}}{J_1[2\sqrt{2(-b_{control})^{\frac{1}{2}}}] / \sqrt{2(-b_{control})^{\frac{1}{2}}}}$ represents the contribu-

tion from electric field and $e^{-\frac{\Delta E_a}{kT}}$ represents the effect of activation energy changes on k_{diss} . We first discuss the improvement of k_{diss} caused by the internal electric field change after doping at the heterojunction. The slightly improved internal electric field due to V_{bi} improvement, from 1.02 to 1.06 V, as discussed above, leads to 9.0% increment of k_{diss} after heterojunction doping.

On the other hand, we extract the E_a from $J_{sc}-1/T$ plot (Figure 4a,b) according to the Arrhenius equation:

$$J_{sc} = J_0 \exp\left(-\frac{E_a}{kT}\right) \quad (6)$$

where J_0 is the pre-exponential factor, and E_a is the activation energy reflecting the energy required for the geminate pair separation if bimolecular recombination is negligible, as in PHJ devices.^[29,63] We stress that E_a may be underestimated because J_{sc} is obtained with built-in potential. The less significant temperature dependence of J_{sc} produces lower E_a of 4.28 meV for the heterojunction doped PHJ device, comparing to that of 782 meV for the control PHJ device at 1 Sun (Figure 4a and Figure S14, Supporting Information). The lower E_a of the doped devices suggests easier charge separation than control devices, which benefits both J_{sc} and FF. Quantitatively, $\Delta E_a = 3.54$ meV gives additional k_{diss} increment of 14.7%. The combined effects of internal electric field and activation energy lead to 25% overall k_{diss} increment, that is, $k_{diss,doped} = 1.25k_{diss,control}$. Combining with the IQE measurements, an increment of 20% in exciton dissociation probability (P) was obtained, which matches with the experimentally measured J_{sc} improvement very well.

2.6. Effect of Heterojunction Doping on Activation Energy

Although aware of yet rarely studied, it is important to understand the underlying mechanism of doping on E_a for exciton dissociation and photocharge generation. Obviously, besides the energy level offset (which relates with the internal electric

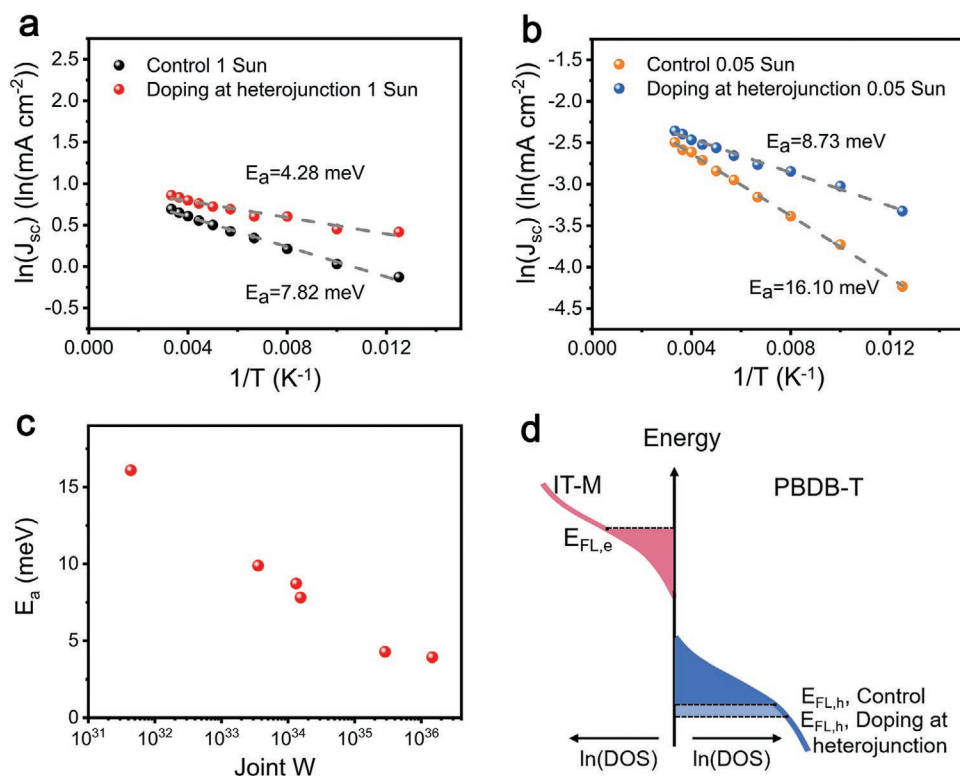


Figure 4. a) Plots of J_{sc} as a function of temperature for PBDB-T/IT-M devices under 1 Sun irradiation. b) Plots of J_{sc} as a function of temperature for PBDB-T/IT-M PHJ devices under 0.05 Sun irradiation. c) Plots of E_a from experiments as a function of DOS. d) Sketch of the occupancy of PBDB-T HOMO DOS and IT-M LUMO DOS in PHJ devices under 1 Sun irradiation.

field), the other major difference between the control and doped heterojunction lays in the Fermi level, namely the corresponding occupancy of density of states (DOS_{FL}). To understand the effect of DOS on E_a , we here take the entropy in Gibbs free energy change into considerations:

$$\Delta G = -\frac{e}{4\pi\epsilon_0\epsilon_r} \left(\frac{1}{r} - \frac{1}{r_0} \right) - k_B T \ln \left(\frac{W}{W_0} \right) \quad (7)$$

where the first term represents for the change in Coulomb binding energy, and the second term represents for the entropy driving force for CT exciton dissociation.^[27–30] Here, W represents for the electronic degeneracy, that is, the molecular states available to accommodate electrons and holes (DOS_{FL}); ϵ_0 and ϵ_r are the vacuum permittivity and the relative dielectric constant respectively; and r is the initial electron–hole distance of the CT exciton. For doped heterojunction, we estimate the local carrier density to be $\approx 5 \times 10^{16} \text{ cm}^{-3}$ using simple parallel capacitor model (with $\Delta E = 80$ mV as indicated in Figure 1e,f). The carrier density is obviously higher than the illuminated carrier density in the control device, which is typically below $2 \times 10^{16} \text{ cm}^{-3}$ under 1 Sun irradiation.^[64] Conceptually, the larger DOS_{FL} correlates to easier CT exciton dissociation according to the entropy term in the free energy formula.

To confirm the effect of joint W ($W = \text{DOS}_{FL,h} \times \text{DOS}_{FL,e}$) on CT exciton separation, we conducted low illumination measurements on the PHJ devices (Figure 4b and Figure S15, Supporting Information) and BHJ device (Figure S16,

Supporting Information). The illumination intensity affects the quasi-Fermi level and W of both electrons and holes within the device. We used a standard DOS model with Gaussian distribution (peak of site density: $5.0 \times 10^{20} \text{ cm}^{-3} \text{ eV}^{-1}$ located at $-/+0.15$ eV away from HOMO/LUMO, respectively; $\sigma = 0.075$ eV). The DOS_{FL} was calculated by $n = \int_{-\infty}^{E_{f,n}} \text{DOS}_n(E) \times f_n(E, T) dE$ and $p = \int_{E_{f,p}}^{+\infty} \text{DOS}_p(E) \times f_p(E, T) dE$,

where $f(E, T)$ represents for the Fermi–Dirac distribution. Drift-diffusion simulation shows the free electron and hole carrier density in BHJ under 1 Sun illumination is $\approx 2 \times 10^{16} \text{ cm}^{-3}$, which gives $\text{DOS}_{FL,n}$ and $\text{DOS}_{FL,p}$ as $1.21 \times 10^{18} \text{ cm}^{-3} \text{ eV}^{-1}$.^[65] The $\text{DOS}_{FL,n}$ and $\text{DOS}_{FL,p}$ under other conditions are calculated in the same way. As illumination intensity decreases from 1 Sun to 0.05 Sun, E_a of the doped device increases by 4.45 meV (from 4.28 to 8.73 meV). However, in the control device, E_a increases by 8.28 meV (from 7.82 to 16.10 meV), which is nearly twofold of the E_a increment of the doped device. This phenomenon correlates the DOS_{FL} with E_a , namely higher DOS_{FL} produces lower E_a . Notably, it also fits well with the efficient BHJ devices, where the E_a increases from 3.93 to 9.89 meV when light intensity decreased from 1 Sun to 0.05 Sun (Figure S16, Supporting Information). The relation of E_a and the corresponding joint W is shown in Figure 4c (Table S5, Supporting Information), with a sketch of DOS changes under varied illuminations as illustrated in Figure 4d. As displayed, our experimental E_a values obey good linear relation with the DOS entropy $\ln W$.

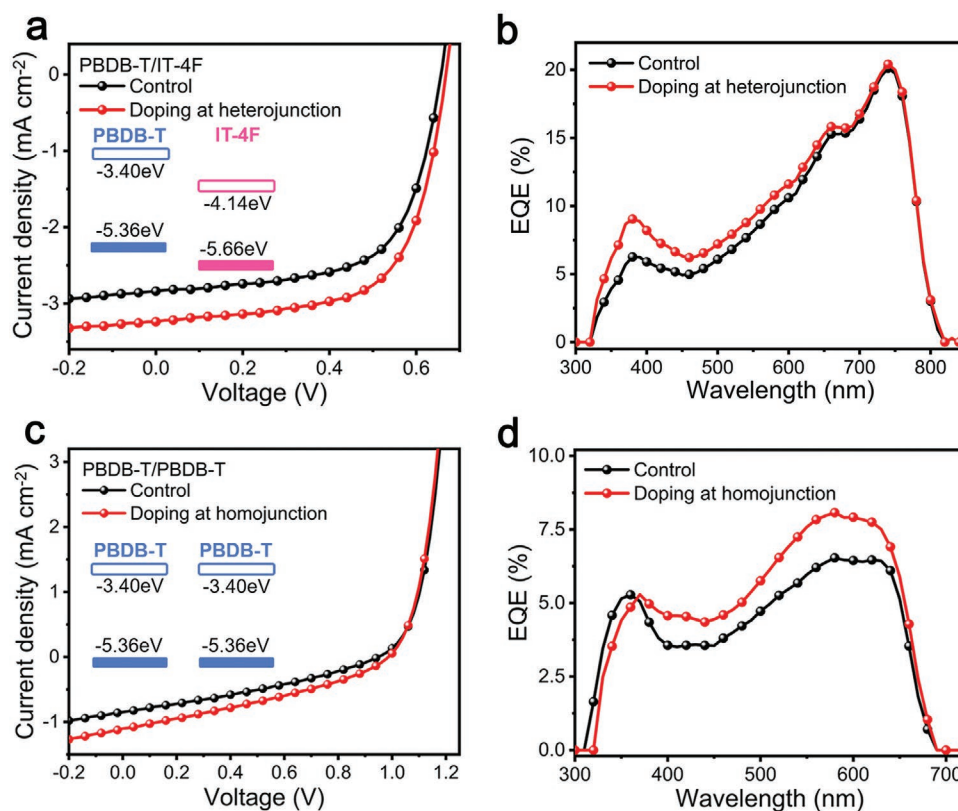


Figure 5. a,b) Photovoltaic performances of PBDB-T/IT-4F PHJ devices: J - V curves (a) and the corresponding EQE curves (b). c,d) Photovoltaic performances of PBDB-T homojunction PHJ devices: J - V curves (c) and the corresponding EQE curves (d). The insets in (a) and (c) are the schemes of PHJ devices.

Heterojunction doping in this work effectively increases the occupancy of PBDB-T HOMO $\text{DOS}_{\text{FL,h}}$, thus it reduces the entropy-driven activation energy for CT state dissociation. However, despite a good linear relationship between E_a and $\ln W$, it has to be noted that ΔG does not simply correlates to ΔE_a in Equation (6). For example, when W increases by tenfold, ΔG decreases by 0.06 eV, while E_a decreases by 0.003 eV only. Though the specific mechanism between the DOS entropy and E_a requires further investigations, the result clearly indicates an entropy-related mechanism that determines E_a and thus carrier generation, and one can apply interface doping strategy to effectively reduce E_a and increase charge generation efficiency.

2.7. The Generality Examination

As a methodology of the D/A heterojunction modifications to enhance the photovoltaic performance, the general nature of this approach is of utmost importance. In order to determine the applicability to other material combinations, we tested on additional PHJ devices with larger or zero driving force for photocharge generation. We first used 3,9-bis(2-methylene-((3-(1,1-dicyanomethylene)-6,7-difluoro)indanone))-5,5,11,11-tetrakis(4-hexylphenyl)-dithieno[2,3-d':3'-d'']-s-indaceno[1,2-b:5,6-b']dithiophene (IT-4F) to replace IT-M (Figure S1, Supporting Information). With a deeper LUMO level of -4.14 eV, the LUMO offset increases from 0.57 eV of

PBDB-T/IT-M to 0.73 eV of PBDB-T/IT-4F (inset of Figure 5a). When inserting an ultrathin dopant layer of F6TCNNQ, we observe enhancements in all three parameters (Figure 5a,b, and Table 2). The largest improvement still comes from J_{sc} , which increases from average 2.87 to 3.18 mA cm^{-2} , contributing to a PCE increase by 13%. The enhanced PCE with larger LUMO offset manifests that the significant role of heterojunction doping cannot be vanished by simply tuning the molecular energy level. Furthermore, we studied the case with zero LUMO and HOMO offsets by fabricating the PBDB-T/PBDB-T homojunction PHJ devices (inset of Figure 5c). Surprisingly, adding a dopant layer improves the average J_{sc} from 0.83 to 1.03 mA cm^{-2} . Notably, the V_{oc} increases by 0.026 V on the top of a high value of 0.939 V (Figure 5c,d, and Table 2). The homojunction device results demonstrate the great potential of heterojunction doping in the material systems with low driving force which hold the efficiency records nowadays.

3. Conclusion

In conclusion, this work presents a D/A heterojunction doping strategy to modify the interface energy diagrams. We find that heterojunction doping improves all three photovoltaic parameters, especially J_{sc} , in a model PHJ system. The effects of traditional roles of a thin layer are excluded consecutively, including the e-h pair distance, dipole modification, and the

Table 2. Photovoltaic performances of PBDB-T/IT-4F and PBDB-T/PBDB-T in PHJ device structure (The average values are obtained from 10 devices).

Conditions		$V_{oc\ max}$ [V]	$V_{oc\ avg}$ [V]	FF_{max} [%]	FF_{avg} [%]	$J_{sc\ max}$ [mA cm ⁻²]	$J_{sc\ avg}$ [mA cm ⁻²]	PCE_{max} [%]	PCE_{avg} [%]
PBDB-T/IT-4F	Control	0.66	0.65 ± 0.006	63.8	63.4 ± 0.8	2.84	2.87 ± 0.03	1.18	1.18 ± 0.02
	Doped	0.67	0.66 ± 0.006	64.1	63.8 ± 1.1	3.24	3.18 ± 0.04	1.38	1.33 ± 0.03
PBDB-T/PBDB-T	Control	0.95	0.94 ± 0.030	31.8	33.6 ± 2.7	0.85	0.83 ± 0.04	0.26	0.26 ± 0.03
	Doped	0.98	0.97 ± 0.020	34.8	34.1 ± 2.1	1.17	1.03 ± 0.06	0.40	0.34 ± 0.03

optical spacer. The estimation on detailed voltage loss reveals that the upward CT state movement and reduced non-radiative recombination are responsible for the V_{oc} increment. The J_{sc} increment originates from the facilitated dissociation of CT exciton, due to the combined effects of increased internal electric field and reduced activation energy. The reduced activation energy by heterojunction doping is further correlated with the DOS entropy. This is the first in-device demonstration to increase charge separation efficiency through an entropy-related mechanism. We also extend the application scope to homojunction devices. The surprising performance enhancement in homojunction device reveals the great potentials of electronic doping to overcome the paradox between the high J_{sc} and V_{oc} in OPVs. Herein, we stress the electronic doping as the third route to facilitating charge generation for OPV in addition to the commonly used strategies via tedious and complicated molecular structure modifications and device architecture engineering. We expect further that the heterojunction doping can make a more significant performance improvement when combining with the cascade electronic structure.^[66] A charge-cascade interlayer of either conjugated polymer or polyelectrolyte enhances the photocurrent by broadening the photo-response range, suppressing the charge recombination, or tuning the dielectric constant.^[67,68] Alternatively, incorporating a low-bandgap polymer into the D/A blend increases photocurrent by enlarging the exciton diffusion length via Förster resonance energy transfer.^[69,70] In the meantime, future studies will also include the fundamental understanding and applications of the entropy-related mechanism.

4. Experimental Section

Materials: PBDB-T, IT-M, and IT-4F were purchased from Solarmer Materials Inc. F6TCNNQ was purchased from Lumtec Inc. Zinc acetate dihydrate, ethanalamine, 2-methoxyethanol, chloroform (CF), molybdenum oxide, and ethanol were purchased from Sigma-Aldrich. All chemicals in the experiments were used as received.

Device Fabrication: The PHJ organic solar cells were fabricated with an inverted device configuration of ITO/ZnO/Active Layer/MoO₃/Al. The ITO substrates were cleaned by sequential sonication in deionized water, acetone, and isopropanol for 20 min of each step, and then dried by nitrogen flow. After UVO treatment for 20 min, a ZnO precursor solution (dissolving zinc acetate dihydrate in 2-methoxyethanol with ethanalamine) was spin-coated on the ITO substrates at 4500 rpm for 30 s, followed by thermal annealing at 200 °C for 30 min to form an electron-transporting layer. The donor PBDB-T (5 mg mL⁻¹) and acceptor IT-M, IT-4F (10 mg mL⁻¹) were dissolved into CF, respectively. The active layer was fabricated by the floating-film-transfer method. The polymer donor was spin-coated onto the PEDOT:PSS layer after well dissolved to produce a ≈30 nm thick layer and then floated in water. The acceptor

solution was spin-coated on ZnO substrate to form a ≈30 nm layer and then scooped up the donor layer. After placing the samples in vacuum overnight, 10 nm MoO₃/100 nm Al were sequentially deposited by thermal evaporation as the anode at a vacuum level under 1×10^{-4} Pa. The effective area of solar cells was 0.04 cm².

Fourier Transform Infrared Spectroscopy, Ultraviolet–Visible Near-Infrared Spectroscopy, and Ultraviolet Photoelectron Spectroscopy: FTIR was performed on a Bruker Alpha II spectrometer. The shifts toward lower wavenumber of the characteristic C≡N bands indicate the negatively charged state of F6TCNNQ. The UV–vis NIR spectra were collected on a Shimadzu UV-3600 Plus. UPS spectra were acquired on ESCALAB Xi+ (Thermo Fisher).

Kelvin Probe Force Microscopy: KPFM images were obtained by a commercial SPM system (MFP3D, Oxford Instruments, USA). The surface potential was defined as $(\Phi_{tip} - \Phi_{sample})/e$. The conductive probe tip used in the measurements was Pt coated.

Optical Transfer-Matrix Model: In order to study the optical physical behavior of OPVs, a numerical simulation based on the optical transfer-matrix model was adopted. Upon simplifying the device structure as multiple thin sublayers, one could deduce the distribution of the optical electric field by considering the reflection at the interfaces and the transmission inside the sublayers. After that, assuming the device was working under the AM 1.5G condition, the time-average monochromatic energy dissipation was obtained as a function of position (x) according to the following equation:

$$Q(x, \lambda) = \frac{2\pi\epsilon_0 c k n |E(x, \lambda)|^2}{\lambda} \quad (8)$$

where ϵ_0 was the permittivity of vacuum, c was the speed of light, k was the extinction coefficient (calculated by absorbance), n was the refractive index (set as 2), $E(x, \lambda)$ was the optical electric field at an arbitrary position x , and λ was the monochromatic wavelength. The value of k was calculated by the formula:

$$A(\lambda) = \lg\left(\frac{I_0}{I}\right) = -\lg(e^{-4\pi k d / \lambda}) \quad (9)$$

where d was the film thickness. Note that, the calculated time-average monochromatic energy dissipation should be integrated within the whole light absorption range, and the wavelength range of 330–1000 nm was adopted to perform discrete integration.

J–V Characteristics and Temperature Dependence of J–V Characteristics: The J–V curves were tested in the N₂ glovebox under AM 1.5G (100 mW cm⁻²) using an AAA solar simulator (SS-F5-3A, Enli Technology Co., Ltd.) calibrated with a standard photovoltaic cell equipped with KG5 filter and a Keithley 2400 source meter. The temperature-dependent J–V curves were tested under high vacuum conditions. The sample temperature was controlled by the TC 202 temperature controller ranging from 80 to 300 K. The J–V characteristics measurements were performed under the illumination of an AM 1.5 G solar simulator (100 mW cm⁻²).

External Quantum Efficiency Measurements: The EQE curves were obtained by Solar Cell Spectral Response Measurement System QE-R3018 (Enli Technology Co., Ltd.), and the standard Si photovoltaic cell was employed to calibrate the light intensity.

Photoluminescence and Time-Resolved Photoluminescence: The steady PL spectra measurements were performed using a HORIBA DeltaFlex system (HORIBA) with an excitation wavelength at 510 nm. The TRPL spectra were acquired with a time-correlated single-photon counting method using an Edinburgh Instruments FLS920 fluorescence spectrometer.

Grazing Incident Wide-Angle X-Ray Scattering: GIWAXS measurements were performed on Xeuss 2.0 small angle X-ray scatterometer with MetalJet-D2 X-ray source. Thin-film samples were spin-casted onto Si substrates. The scattering signal was recorded by a 2D detector (Pilatus 3R 1M) with a pixel size of 0.172 mm by 0.172 mm. The incidence angle was chosen as 0.2°, which gave the optimized signal-to-background ratio. The beam energy was 9.4 keV. Typically, the exposure of 30 min was conducted for each image acquisition and two images were combined to eliminate the detector gaps. Data processing was carried out using the NIKA software package.

Sensitive External Quantum Efficiency and EQE_{EL} Measurement: For the sEQE measurement, the light from halogen light source (LSH-75, Newport) became monochromatic light by using a monochromator (CS260-RG-3-MC-A, Newport), and was focused on the device to generate electrical signals. Then the signals were amplified by the front-end current amplifier (SR570, Stanford) and finally collected by the phase-locked amplifier (Newport). The EQE spectrum was obtained by using the corrected Si standard detector (S1337-1010Br). The EQE_{EL} measurement system included a Keithley 2400 digital source meter, Keithley 6482 picoammeters, and a standard Si detector (S1337-1010Br).

Transient Photovoltage: For the TPV measurements, the background illumination was provided by a normal LED light source, and the pulsed light was provided by arbitrary wave generator (AFG322C, Tektronix). The TPV signals for the device were collected by an oscilloscope (MDO4104C, Tektronix).

Supporting Information

Supporting Information is available from the Wiley Online Library or from the author.

Acknowledgements

Thanks for the support from the National Natural Science Foundation of China (21975198, 51803162, and 21875182), the Ministry of Science and Technology (2016YFA0200700), the Fundamental Research Funds for the Central Universities (ZZ201805178), and 111 project 2.0 (BP2018008). This work was supported by the Open Fund of the State Key Laboratory of Luminescent Materials and Devices (South China University of Technology).

Conflict of Interest

The authors declare no conflict of interest.

Data Availability Statement

Research data are not shared.

Keywords

entropies, exciton dissociation, molecular doping, non-radiative recombination, organic heterojunctions, organic solar cells

Received: March 1, 2021
Revised: March 20, 2021
Published online: April 17, 2021

- [1] F. Zhao, C. Wang, X. Zhan, *Adv. Energy Mater.* **2018**, *8*, 1703147.
- [2] T. M. Clarke, J. R. Durrant, *Chem. Rev.* **2010**, *110*, 6736.
- [3] T. F. Hinrichsen, C. C. S. Chan, C. Ma, D. Paleček, A. Gillett, S. Chen, X. Zou, G. Zhang, H. L. Yip, K. S. Wong, R. H. Friend, H. Yan, A. Rao, P. C. Y. Chow, *Nat. Commun.* **2020**, *11*, 5617.
- [4] V. Coropceanu, X. K. Chen, T. Wang, Z. Zheng, J. L. Brédas, *Nat. Rev. Mater.* **2019**, *4*, 689.
- [5] K. Vandewal, S. Albrecht, E. T. Hoke, K. R. Graham, J. Widmer, J. D. Douglas, M. Schubert, W. R. Mateker, J. T. Bloking, G. F. Burkhard, A. Sellinger, J. M. J. Fréchet, A. Amassian, M. K. Riede, M. D. McGehee, D. Neher, A. Salleo, *Nat. Mater.* **2014**, *13*, 63.
- [6] A. Y. Sosorev, D. Y. Godovsky, D. Y. Paraschuk, *Phys. Chem. Chem. Phys.* **2018**, *20*, 3658.
- [7] H. Tamura, I. Burghardt, *J. Am. Chem. Soc.* **2013**, *135*, 16364.
- [8] G. Grancini, M. Maiuri, D. Fazzi, A. Petrozza, H. J. Egelhaaf, D. Brida, G. Cerullo, G. Lanzani, *Nat. Mater.* **2013**, *12*, 29.
- [9] S. D. Dimitrov, A. A. Bakulin, C. B. Nielsen, B. C. Schroeder, J. Du, H. Bronstein, I. McCulloch, R. H. Friend, J. R. Durrant, *J. Am. Chem. Soc.* **2012**, *134*, 18189.
- [10] A. E. Jailaubekov, A. P. Willard, J. R. Tritsch, W. L. Chan, N. Sai, R. Gearba, L. G. Kaake, K. J. Williams, K. Leung, P. J. Rossky, X. Y. Zhu, *Nat. Mater.* **2013**, *12*, 66.
- [11] L. Perdigón-Toro, H. Zhang, A. Markina, J. Yuan, S. M. Hosseini, C. M. Wolff, G. Zuo, M. Stolterfoht, Y. Zou, F. Gao, D. Andrienko, S. Shoaee, D. Neher, *Adv. Mater.* **2020**, *32*, 1906763.
- [12] J. Kurpiers, T. Ferron, S. Roland, M. Jakob, T. Thiede, F. Jaiser, S. Albrecht, S. Janietz, B. A. Collins, I. A. Howard, D. Neher, *Nat. Commun.* **2018**, *9*, 2038.
- [13] K. Vandewal, S. Albrecht, E. T. Hoke, K. R. Graham, J. Widmer, J. D. Douglas, M. Schubert, W. R. Mateker, J. T. Bloking, G. F. Burkhard, A. Sellinger, J. M. J. Fréchet, A. Amassian, M. K. Riede, M. D. McGehee, D. Neher, A. Salleo, *Nat. Mater.* **2014**, *13*, 63.
- [14] Z. Wang, Z. Peng, Z. Xiao, D. Seyitliyev, K. Gundogdu, L. Ding, H. Ade, *Adv. Mater.* **2020**, *32*, 2005386.
- [15] K. Nakano, Y. Chen, B. Xiao, W. Han, J. Huang, H. Yoshida, E. Zhou, K. Tajima, *Nat. Commun.* **2019**, *10*, 2520.
- [16] A. Karki, J. Vollbrecht, A. L. Dixon, N. Schopp, M. Schrock, G. N. M. Reddy, T. Q. Nguyen, *Adv. Mater.* **2019**, *31*, 1903868.
- [17] Z. Luo, T. Liu, Y. Wang, G. Zhang, R. Sun, Z. Chen, C. Zhong, J. Wu, Y. Chen, M. Zhang, Y. Zou, W. Ma, H. Yan, J. Min, Y. Li, C. Yang, *Adv. Energy Mater.* **2019**, *9*, 1900041.
- [18] S. Karuthedath, J. Gorenflot, Y. Firdaus, N. Chaturvedi, C. S. P. De Castro, G. T. Harrison, J. I. Khan, A. Markina, A. H. Balawi, T. A. D. Peña, W. Liu, R. Z. Liang, A. Sharma, S. H. K. Paleti, W. Zhang, Y. Lin, E. Alarousu, D. H. Anjum, P. M. Beaujuge, S. De Wolf, I. McCulloch, T. D. Anthopoulos, D. Baran, D. Andrienko, F. Laquai, *Nat. Mater.* **2021**, *20*, 378.
- [19] M. Schwarze, K. S. Schellhammer, K. Ortstein, J. Benduhn, C. Gaul, A. Hinderhofer, L. P. Toro, R. Scholz, J. Kublitski, S. Roland, M. Lau, C. Poelking, D. Andrienko, G. Cuniberti, F. Schreiber, D. Neher, K. Vandewal, F. Ortman, K. Leo, *Nat. Commun.* **2019**, *10*, 2466.
- [20] G. Zhang, X. K. Chen, J. Xiao, P. C. Y. Chow, M. Ren, G. Kupgan, X. Jiao, C. C. S. Chan, X. Du, R. Xia, Z. Chen, J. Yuan, Y. Zhang, S. Zhang, Y. Liu, Y. Zou, H. Yan, K. S. Wong, V. Coropceanu, N. Li, C. J. Brabec, J. L. Brédas, H. L. Yip, Y. Cao, *Nat. Commun.* **2020**, *11*, 3943.
- [21] F. J. Kahle, C. Saller, S. Olthof, C. Li, J. Lebert, S. Weiß, E. M. Herzog, S. Hüttner, K. Meerholz, P. Strohrriegel, A. Köhler, *J. Phys. Chem. C* **2018**, *122*, 21792.
- [22] S. T. Hoffmann, F. Jaiser, A. Hayer, H. Bässler, T. Unger, S. Athanasopoulos, D. Neher, A. Köhler, *J. Am. Chem. Soc.* **2013**, *135*, 1772.
- [23] A. Köhler, D. A. dos Santos, D. Beljonne, Z. Shuai, J. L. Brédas, A. B. Holmes, A. Kraus, K. Müllen, R. H. Friend, *Nature* **1998**, *392*, 903.

- [24] A. Karki, G. J. A. H. Wetzelaer, G. N. M. Reddy, V. Nádaždy, M. Seifrid, F. Schauer, G. C. Bazan, B. F. Chmelka, P. W. M. Blom, T. H. Nguyen, *Adv. Funct. Mater.* **2019**, *29*, 1901109.
- [25] H. Bässler, A. Köhler, *Phys. Chem. Chem. Phys.* **2015**, *17*, 28451.
- [26] J. C. Blakesley, D. Neher, *Phys. Rev. B* **2011**, *84*, 075210.
- [27] T. R. Kafle, B. Kattel, S. Wanigasekara, T. Wang, W. L. Chan, *Adv. Energy Mater.* **2020**, *10*, 1904013.
- [28] M. Stolterfoht, A. Armin, S. Shoaee, I. Kassal, P. Burn, P. Meredith, *Nat. Commun.* **2016**, *7*, 11944.
- [29] F. Gao, W. Tress, J. Wang, O. Inganäs, *Phys. Rev. Lett.* **2015**, *114*, 128701.
- [30] B. A. Gregg, *J. Phys. Chem. Lett.* **2011**, *2*, 3013.
- [31] Y. Dong, V. C. Nikolis, F. Talnack, Y. C. Chin, J. Benduhn, G. Londi, J. Kublitski, X. Zheng, S. C. B. Mannsfeld, D. Spoltore, L. Muccioli, J. Li, X. Blase, D. Beljonne, J. S. Kim, A. A. Bakulin, G. D'Avino, J. R. Durrant, K. Vandewal, *Nat. Commun.* **2020**, *11*, 4617.
- [32] N. A. Ran, S. Roland, J. A. Love, V. Savikhin, C. J. Takacs, Y. T. Fu, H. Li, V. Coropceanu, X. Liu, J. L. Brédas, G. C. Bazan, M. F. Toney, D. Neher, T. Q. Nguyen, *Nat. Commun.* **2017**, *8*, 79.
- [33] S. Sweetnam, K. R. Graham, G. O. N. Ndjawa, T. Heumüller, J. A. Bartelt, T. M. Burke, W. Li, W. You, A. Amassian, M. D. McGehee, *J. Am. Chem. Soc.* **2014**, *136*, 14078.
- [34] J. D. Zimmerman, X. Xiao, C. K. Renshaw, S. Wang, V. V. Diev, M. E. Thompson, S. R. Forrest, *Nano Lett.* **2012**, *12*, 4366.
- [35] I. E. Jacobs, A. J. Moulé, *Adv. Mater.* **2017**, *29*, 1703063.
- [36] X. Xu, L. Yu, H. Yan, R. Li, Q. Peng, *Energy Environ. Sci.* **2020**, *13*, 4381.
- [37] H. Yan, Y. Tang, X. Sui, Y. Liu, B. Gao, X. Liu, S. F. Liu, J. Hou, W. Ma, *ACS Energy Lett.* **2019**, *4*, 1356.
- [38] H. Yan, J. G. Manion, M. Yuan, F. P. G. de Arquer, G. R. McKeown, S. Beaupré, M. Leclerc, E. H. Sargent, D. S. Seferos, *Adv. Mater.* **2016**, *28*, 6491.
- [39] Y. Lin, M. I. Nugraha, Y. Firdaus, A. D. Scaccabarozzi, F. Aniés, A. H. Emwas, E. Yengel, X. Zheng, J. Liu, W. Wahyudi, E. Yarali, H. Faber, O. M. Bakr, L. Tsetseris, M. Heeney, T. D. Anthopoulos, *ACS Energy Lett.* **2020**, *5*, 3663.
- [40] D. Zhang, Q. Li, J. Zhang, J. Wang, X. Zhang, R. Wang, J. Zhou, Z. Wei, C. Zhang, H. Zhou, Y. Zhang, *ACS Appl. Mater. Interfaces* **2019**, *12*, 667.
- [41] Z. Chen, Y. Tang, B. Lin, H. Zhao, T. Li, T. Min, H. Yan, W. Ma, *ACS Appl. Mater. Interfaces* **2020**, *12*, 25115.
- [42] Y. Tang, B. Lin, H. Zhao, T. Li, W. Ma, H. Yan, *ACS Appl. Mater. Interfaces* **2020**, *12*, 13021.
- [43] H. Yan, J. Chen, K. Zhou, Y. Tang, X. Meng, X. Xu, W. Ma, *Adv. Energy Mater.* **2018**, *8*, 1703672.
- [44] H. Méndez, G. Heimel, S. Winkler, J. Frisch, A. Opitz, K. Sauer, B. Wegner, M. Oehzelt, C. Röthel, S. Duhm, D. Többens, N. Koch, I. Salzmann, *Nat. Commun.* **2015**, *6*, 8560.
- [45] M. L. Tietze, J. Benduhn, P. Pahner, B. Nell, M. Schwarze, H. Kleemann, M. Krammer, K. Zojer, K. Vandewal, K. Leo, *Nat. Commun.* **2018**, *9*, 1182.
- [46] H. Méndez, G. Heimel, A. Opitz, K. Sauer, P. Barkowski, M. Oehzelt, J. Soeda, T. Okamoto, J. Takeya, J. B. Arlin, J. Y. Balandier, Y. Geerts, N. Koch, I. Salzmann, *Angew. Chem.* **2013**, *125*, 7905.
- [47] I. Salzmann, G. Heimel, S. Duhm, M. Oehzelt, P. Pingel, B. M. George, A. Schnegg, K. Lips, R. P. Blum, A. Vollmer, N. Koch, *Phys. Rev. Lett.* **2012**, *108*, 035502.
- [48] Z. Hu, Z. Zhong, Y. Chen, C. Sun, F. Huang, J. Peng, J. Wang, Y. Cao, *Adv. Funct. Mater.* **2016**, *26*, 129.
- [49] Z. Cui, J. Sun, D. Landerer, C. Sprau, R. Thelen, A. Colsmann, H. Hölscher, W. Ma, L. Chi, *Adv. Mater. Interfaces* **2016**, *3*, 1600446.
- [50] S. Sampat, A. D. Mohite, B. Crone, S. Tretiak, A. V. Malko, A. J. Taylor, D. A. Yarotski, *J. Phys. Chem. C* **2015**, *119*, 1286.
- [51] Y. Zhong, A. Tada, S. Izawa, K. Hashimoto, K. Tajima, *Adv. Energy Mater.* **2014**, *4*, 1301332.
- [52] S. Izawa, K. Nakano, K. Suzuki, K. Hashimoto, K. Tajima, *Adv. Mater.* **2015**, *27*, 3025.
- [53] K. S. Nalwa, J. A. Carr, R. C. Mahadevapuram, H. K. Kodali, S. Bose, Y. Chen, J. W. Petrich, B. Ganapathysubramanian, S. Chaudhary, *Energy Environ. Sci.* **2012**, *5*, 7042.
- [54] A. Tada, Y. Geng, Q. Wei, K. Hashimoto, K. Tajima, *Nat. Mater.* **2011**, *10*, 450.
- [55] J. Y. Kim, S. H. Kim, H. H. Lee, K. Lee, W. Ma, X. Gong, A. J. Heeger, *Adv. Mater.* **2006**, *18*, 572.
- [56] J. D. Kotlarski, P. W. M. Blom, L. J. A. Koster, M. Lenas, L. H. Slooff, *J. Appl. Phys.* **2008**, *103*, 084502.
- [57] L. A. A. Pettersson, L. S. Roman, O. Inganäs, *J. Appl. Phys.* **1999**, *86*, 487.
- [58] J. K. Tan, R. Q. Png, C. Zhao, P. K. H. Ho, *Nat. Commun.* **2018**, *9*, 3269.
- [59] S. Liu, J. Yuan, W. Deng, M. Luo, Y. Xie, Q. Liang, Y. Zou, Z. He, H. Wu, Y. Cao, *Nat. Photonics* **2020**, *14*, 300.
- [60] K. Vandewal, K. Tvingstedt, A. Gadisa, O. Inganäs, J. V. Manca, *Phys. Rev. B* **2010**, *81*, 125204.
- [61] Y. Wang, D. Qian, Y. Cui, H. Zhang, J. Hou, K. Vandewal, T. Kirchartz, F. Gao, *Adv. Energy Mater.* **2018**, *8*, 1801352.
- [62] C. L. Braun, *J. Chem. Phys.* **1984**, *80*, 4157.
- [63] I. Riedel, V. Dyakonov, *Phys. Status Solidi A* **2004**, *201*, 1332.
- [64] Z. Shang, T. Heumueller, R. Prasanna, G. F. Burkhard, B. D. Naab, Z. Bao, M. D. McGehee, A. Salleo, *Adv. Energy Mater.* **2016**, *6*, 1601149.
- [65] M. L. Tietze, L. Burtone, M. Riede, B. Lüssem, K. Leo, *Phys. Rev. B* **2012**, *86*, 035320.
- [66] K. Nakano, K. Tajima, *Adv. Mater.* **2017**, *29*, 1603269.
- [67] Z. K. Tan, K. Johnson, Y. Vaynzof, A. A. Bakulin, L. L. Chua, P. K. H. Ho, R. H. Friend, *Adv. Mater.* **2013**, *25*, 4131.
- [68] A. Kumar, G. Pace, A. A. Bakulin, J. Fang, P. K. H. Ho, W. T. S. Huck, R. H. Friend, N. C. Greenham, *Energy Environ. Sci.* **2013**, *6*, 1589.
- [69] M. Koppe, H. J. Egelhaaf, E. Clodic, M. Morana, L. Lüer, A. Troeger, V. Sgobba, D. M. Guldi, T. Ameri, C. J. Brabec, *Adv. Energy Mater.* **2013**, *3*, 949.
- [70] Y. Wang, H. Ohkita, H. Benten, S. Ito, *ChemPhysChem* **2015**, *16*, 1263.